Automated Mapping of Urban Heat Island to Predict Land Surface Temperature and Land Use/Cover Change Using Machine Learning Algorithms: Mansoura City

Sameh S. [1,2]*, Zarzoura F. [3] and El-Mewafi M. [4]
[1]Faculty of Engineering and Technology, Badr University in Cairo (BUC), Cairo, Egypt
E-mail: sara.sameh@buc.edu.eg
[2]Public Works Engineering Department, Faculty of Engineering, Mansoura University, Mansoura 35516, Egypt, E-mail: sarasameh724@gmail.com
[3]Public Works Engineering Department, Faculty of Engineering, Mansoura University, Mansoura 35516, Egypt, E-mail: fawzihamed@mans.edu.eg
[4]Public Works Engineering Department, Faculty of Engineering, Mansoura University, Mansoura 35516, Egypt, E-mail: mmewafi1@mans.edu.eg
**Corresponding Author*

DOI: https://doi.org/10.52939/ijg.v18i6.2461

Abstract
Urban heat island (UHI) frequency and emergence are strongly associated with variations in land use/land cover (LU/LC) and land surface temperature (LST). This study investigates the impact of LU/LC class changes on LST based on the distribution of UHI spot maps in Mansoura city, Egypt, using Landsat satellite images from 1991 to 2021. Based on these estimated LU/LC and LST maps, machine learning algorithms, cellular automata, and artificial neural network approaches were used to predict future changes in LU/LC and LST for 2031. The influence of UHI may be quantified using the urban thermal field variance index (UTFVI). The geographic information system (GIS) add-in UHI calculator ArcGIS tool was created because we considered the spatial consequences of employing remote sensing data. This tool includes all the methods and procedures for calculating LST and UHI. The analysis revealed a positive correlation between LST and normalized difference built-up index and a negative correlation between LST and normalized difference vegetation index. The forecasted results for 2031 also show that the built-up area will grow roughly 20%, with a considerable drop in vegetation by 18%. If the city's fast urbanization continues, more than 40% of Mansoura will have land surface temperatures above 45°C by 2031. Avoiding dense built-up areas and growing vegetation spaces remain efficient means of minimizing the influence of UTFVI in urban construction practice. Therefore, this research will help to achieve sustainable development by providing essential insights into the complicated interplay between diverse aspects of urban settings and promoting city competency.

Keywords: Artificial Neural Network, Land Surface Temperature, Machine Learning, Prediction, Urban Heat Island

1. Introduction

The world's population is expected to increase by 2 billions in the next 30 years (United Nations). According to estimations, about 90% of this population growth will occur in Asia and Africa, the two continents with the biggest concentrations of impoverished and malnourished people [1]. In this regard, urbanization is anticipated to play a significant role in land use/land cover (LU/LC) shifts, as well as in socioeconomic and environmental areas in developing countries [2].

In this case, urbanization processes significantly impact how Earth's systems behave in developing nations due to natural surroundings, harming ecosystems and biodiversity, and exacerbating consequences of climate change [3]. Additionally, urban growth issues will be severe in developing countries, and urban food insecurity and shortages will impact rural and suburban areas significantly [4].

Thus, to provide employment and accomplish the sustainable development goals (SDGs), developing nations must focus on researching LU/LC dynamics and improving the governance of urban growth [5]. The distribution of LU/LC characteristics is directly connected to the land surface temperature (LST) of urban areas. For example, buildings, roads, grass, parking lots, and cemeteries have thermal, radiative, moisture, and aerodynamic properties connected to their surroundings [6]. Moreover, a decrease in the areas of agricultural land and water and an increase in LST due to the absorption of rays lead to negative impacts of climate change on daily human lives. LST is an indicator of an urban heat island (UHI), which influences development in many sectors. This case study considers UHI, which can be estimated using satellite thermal remote sensing data [7]. As a result, satellite remote sensing provides a method for collecting LST by investigating thermal data. Because UHI relies heavily on LST, several researchers used remotely sensed data to investigate the most appropriate assessment of UHI [7] [8] [9].

Support vector machine (SVM) is a classifier that consists of a collection of related machine-learning algorithms used for regression and classification. The theory of SVM was introduced in [10] and later extended in [11]. Furthermore, SVM has been extensively studied and applied in remote sensing. The classification performance of SVM was higher than that of the maximum likelihood and decision tree algorithms [12]. Yousefi et al. [13] employed Landsat images to test the nine supervised classification techniques: SVM, neural network, Mahalanobis distance, maximum likelihood, redistance, spectral angle mapper, spectral information divergence, parallelepiped, and binary code. They found that the SVM classification technique outperforms other approaches, with a kappa value of 0.9503 and overall accuracy of 90.94%; thereby, inspiring researchers to use this method.

LST is calculated using data recorded from satellite imagery. It takes time and requires high accuracy when using several formulae to derive LST. To overcome this issue, a plug-in tool for the ArcGIS software has been developed to significantly decrease the time and effort required to calculate multiple algorithms. LST retrieval is a complicated process; thus, the ArcGIS plug-in was constructed to simplify and accelerate it [14].

Various land surface indices, such as normalized difference vegetation index (NDVI), normalized difference built-up index (NDBI), normalized difference water index (NDWI), and normalized difference bare soil index (NDBSI), have been widely used to quantify and evaluate the changing characteristics of LST in a mixture of urban areas [15]. Present statistical indices were employed to establish a relationship between LST and various LU/LC types on various land surfaces [16]. Consequently, researchers used remote sensing techniques to analyze the variance of LST in metropolitan areas [17]. Several studies have been conducted to establish thermal comfort indicators for investigating the influence of UHI intensity, such as the temperature humidity index, wet-bulb temperature, physiological equivalent temperature, and urban thermal field variance index(UTFV) [18] [19] [20] [21]. UTFVI index is one of the most widely used indices for evaluating the ecological state of urban areas due to its relationship to LST [22]. Therefore, determining any significant town's environmental confidence level is an important task, especially in urban areas.

LU/LC indices, e.g., NDVI, are less accurate predictors of LST. Comparatively more significant ones are NDBI and NDBSI [23] [24] [25]. Since hypothesis-oriented indicators cannot replicate historical patterns, an artificial neural network (ANN) is the most suitable model for LST simulation. ANN was developed to understand how the human brain functions, and it is constantly developing [26]. No prior knowledge of the components is essential, and its complex design duplicates the steps required within the framework for simulating the rise in potential LST. The multilayer perceptron technology, on which the ANN methodology is based, automatically selects network elements for optimum modeling. In the event of a pattern, the algorithm examines the data and generates a statistic with arbitrarily low accuracy. Then, an automated error function determines the required value by calculating the difference between the random and standard outputs. ANN can be used to predict LST using the LST as the output layer and LU/LC parameters as the hidden layer. Several studies have been conducted in Egypt to investigate UHI and its negative effects on society and the environment. For instance, Effat et al. [27] investigated the dynamics of UHI and used spatial-temporal Landsat data to study the UHI changes across greater Cairo. They found that increasing urban expansion and shortage of agricultural land increased the occurrence of UHIs [27]. El-Fayoum governorate used remote sensing data and geographic information system (GIS) to detect LST [28]. Kamel et al. (2022) investigated the effect of human behavior on UHI in different cities of the El-Menya governorate [29].

Although there are significant numbers of research that models the future LU/LC scenarios, predicting studies for LU/LC and LST are still limited in developing countries. According to previous studies, few researches have been conducted in Mansoura city, Egypt, to forecast the LU/LC classes and their influence on LST. This research aims to investigate the use of remote sensing data to study the spatial and temporal trends in Mansoura city to determine the effect of LU/LC, LST, UHI, and climate changes over the last three decades (1991, 2001, 2011, and 2021). The main objectives of this research are summarized as follows:

1. Assessing a new ArcGIS Python toolset for automated geographic LST and UHI distribution maps for Mansoura city
2. Classifying the LU/LC of Mansoura city using the SVM classifier and categorizing the non-UHI and UHI based on the extracted LST over Mansoura city
3. Investigating the correlation between the LST and LU/LC indices (NDVI, NDBI, NDWI, and NDBSI) for Mansoura city
4. Using UTFVI to determine Mansoura city's thermal comfort level
5. Predicting LST and LU/LC maps for 2031 using ANN-cellar automated algorithm (ANN-CA) to forecast the effect of future LU/LC on climate change in Mansoura city

In developing and improving sustainable ecosystems, this type of analytical research can be significantly used in many sectors to develop sustainable LU/LC management.

2. Materials and Methods

2.1 Field of Study

Mansoura is the capital city of the Dakahlia governorate. Mansoura city, our study area, refers to several districts (e.g., El-Mansoura, Shaha, and Barq El-ezz), as shown in Figure 1. Overlooking the east bank of the Damietta branch of the Nile River. Mansoura city is about 120 km northeast of Cairo capital of Egypt [30]. Mansoura is situated in the northeast of the Nile Delta. It is located between these coordinates: 30.5°–31.5°N and 30°–32° E, with about 322 km^2 total area. Mansoura city's population was about 638,037 people in 2021 (Central Agency for Public Mobilization and Statistics). The surface elevation of Mansoura city is 7 m above the mean sea level. The slope gradient varied from zero to 15%, with an average value of 0.79%, meaning that most of this area is almost flat [30].

In Mansoura city, the highest temperature varies from 45°C in the summer to 20°C in the winter. The lowest temperatures in the summer and winter are 20°C and 7°C, respectively. The total amount of precipitation ranges from 29.2 to 72.3 mm. The study area's geology contains Nile deposits, sabkha deposits, and sand dunes. Vegetation varies from major field crops grown in the summer, such as rice, cotton, and maize, to vegetables, such as tomatoes, potatoes, and cucumbers.

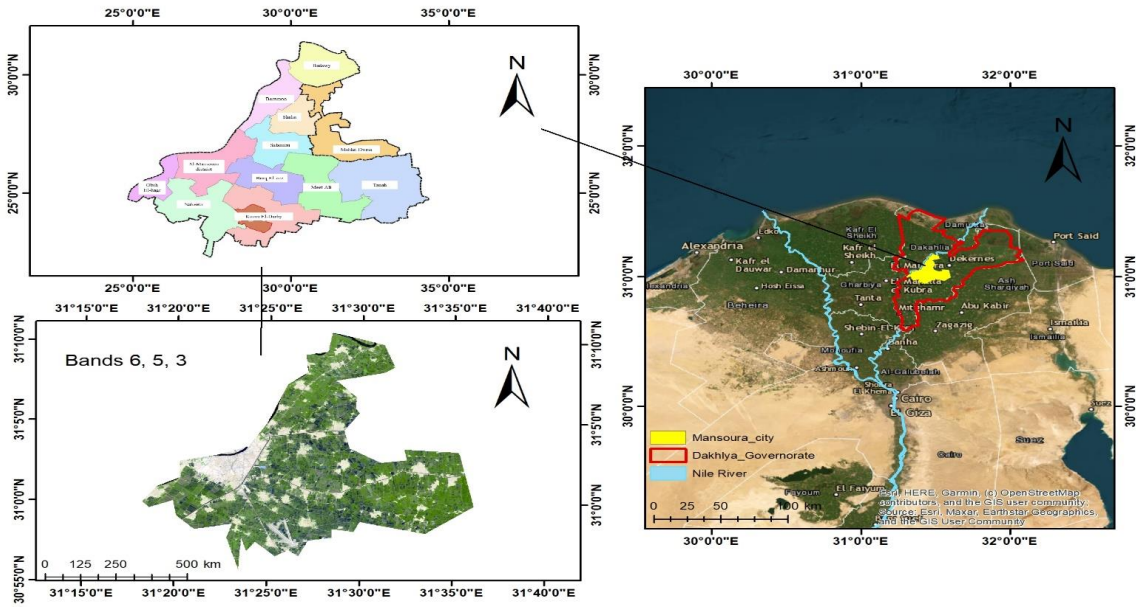

Figure 1: Study area of Mansoura city, Dakahlia governorate, Egypt

Table 1: Data description of satellite images from USGS Earth Explorer for various years

Satellite Data	Type of Sensor	Date of acquisition	Path-Row	Resolution of Thermal bands	Cloud Cover
Landsat 5	(TM) Thematic Mapper	LT05_L1TP_176039_19910722_20180302_01_T1	176-39	120 m (Resampled to 30 m)	Less than 10%
		LT05_L1TP_176039_20010717_20171215_01_T1	176-39		
		LT05_L1TP_176039_20110713_20180312_01_T1	176-39		
Landsat 8	(OLI) Operational Land Imager	LC08_L1TP_176039_20210708_20210713_01_T1	176-39	100 m (Resampled to 30 m)	

2.2 Data Explanation

In this study, we used satellite images from the US Geological Survey (USGS) website, Landsat TM 5 data up to 2013 and afterward Landsat OLI 8 data; https://earthexplorer.usgs.gov/. Table 1 shows the data for 1991, 2001, 2011, and 2021. Landsat 4–5 (thematic mapper (TM)) images consist of seven spectral bands with spatial resolutions of 30 m for bands 1–5 and 7. Band 6 (thermal infrared) spatial resolution is 120 m, and it is resampled to 30-m pixels. In contrast, Landsat 8 consists of nine spectral bands with a spatial resolution of 30 m for bands 1 to 7 and 9; the resolution for band 8 (panchromatic) is 15 m. Thermal bands 10 and 11 are bands with a spatial resolution of 100 m, and it is resampled to 30 m. The Landsat images (Level 1 Terrain Correction Product) were projected to the UTM coordinate system using the WGS-84 data, UTM zone 36 North projection. All Landsat images have been downloaded at a maximum one-month interval to avoid seasonal variation. Images were captured in a cloud-free environment to create LST and LU/LC maps. Image processing and classification were accomplished in ERDAS Imagine 15 and derived LST and UHI distribution maps in ArcMap 10.5 using the UHI ArcGIS Python tool.

2.3 Data Preprocessing

Landsat satellite datasets were used to categorize the geographical distribution of LU/LC classes and estimate LST and UHI for each year. In Landsat 8, separate band images were stacked to be combined, generating a multi-band image. These datasets were converted to 30 m and projected to the WGS 84/UTM zone 36 N. Landsat 5 band 6 and Landsat 8 band10 (thermal infrared band) were used to calculate terrestrial surface temperatures by transforming digital numbers to radiance. This research also investigated NDVI, where bands were used to generate vegetation indices within the spectrum of solar reflections. After preprocessing, the satellite images were used to evaluate UTFVI using the Python tool and ArcGIS 10.5 software. Furthermore, high-resolution Google Earth images were employed as reference data for LU/LC identification.

2.3.1 LU/LC classification using an SVM classifier

Using multispectral data, image classification analyses LU/LC into many classifications. Therefore, many researchers have developed approaches based on supervised and unsupervised classification operations. When identifying training units for image classification, the SVM classifier assigned pixels according to the maximum probability class and implemented the supervised classification method. Using the image classification technique, LU/LC types were classified into four categories: built-up areas, vegetative cover, water bodies, and bare land. The classification technique was performed using the ArcGIS 10.5 software.

2.3.2 Accuracy assessment for LU/LC's SVM data

Approximately 50 samples of ground-based training were produced for each LU/LC class. The classification maps' accuracy was evaluated by overlaying more than 400 random samples of ground truth data from Google Earth images. One of the quantitative methods for evaluating image classification accuracy was used to obtain the kappa statistics, overall accuracy, user accuracy, and producer accuracy [31].

2.3.3 Estimation of different LU/LC indices

NDVI is the most widely used indicator for classifying and assessing vegetation [32]. It negatively affects LST and is also used to calculate LST [33]. Meanwhile, NDBI was used to identify the built-up area [34], and NDWI was used for water area extraction [35]. NDBSI was used to determine bare land [18]. The four indices could be used to categorize various types of LU/LC as in Table 2.

Table 2: Description of the four LU/LC indices

Index	Description	Formulation
NDVI	Normalized difference Vegetation index	$\frac{NIR - RED}{NIR + RED}$
NDBI	Normalized difference build-up index	$\frac{SWIR1 - NIR}{SWIR1 + NIR}$
NDWI	Normalized difference water index	$\frac{GREEN - NIR}{GREEN + NIR}$
NDBSI	Normalized Difference Bare Soil Index	$\frac{(RED + SWIR) - (NIR + BLUE)}{(RED + SWIR) + (NIR + BLUE)}$

2.4 Land Surface Temperature Derivation

2.4.1 A Python tool: UHI calculator for ArcGIS desktop

This tool was created in the Python programming language (version 3.6) and can be run in ArcGIS Desktop, ESRI's comprehensive GIS mapping platform. The goal of creating this tool is to ensure that LST data is obtained fast and precisely, to save time re-entering formulae for various algorithms used during LST computation, and to output several maps from a single operation. This toolbox comprises of the following tools: 1- TOA Radiance, 2_Brightness-Temperature(BT), 3_NDVI-Index, 4_Fractional Vegetation (FV), 5_Emissivity(ε), 6_ LST, 7_ UHI and 8_ (UTFVI). The use Python add-in tool has greatly reduced the human error when adding the formulas for UHI calculations. All formulas used for LST map production have been added to the tool. The LST results from the tool were validated using a manual temperature calculation. Both approaches provide results with a small difference, which is acceptable. Equation (1) transfers a digital number into spectral reflectance for Landsat 8 thermal bands (band 10).

$$\boldsymbol{\rho}\lambda = M_p * Q_{cal} + A_p$$

Equation 1

$\boldsymbol{\rho}_\lambda$ refers to top-of-atmosphere (TOA) spectral reflectance without correction for solar angle (Unit-less), Q_{cal} represents the Level One Pixel in a Digital Number (DN), Mp is the multiplicative scaling factor for the band's reflectance as shown is Equation 1. (REFLECTANCEW_MULT_BAND_n from the metadata), The band's reflectance additive scaling factor is known as Ap. (REFLECTANCE_ADD_BAND_N from the metadata) The following Equation 2 is used to correct the using local sun elevation angles.

$$\boldsymbol{\rho}'\lambda = \frac{\rho\lambda}{sin\theta_s}$$

Equation 2

The thermal band of Landsat 8 imagery, band 10 (10.6 μm -11.19 μm), is used to calculate the land surface temperature [36].

2.4.2 Thermal band DN to brightness temperature tool

Digital number (DN) data for TIR pixel values are first transformed to radiance values. The radiance for Landsat 5 (TM) is calculated using Equation (3) [37].

$$L_\lambda = L_{min} + (L_{max} - L_{min}) * \frac{DN}{255}$$

Equation 3

Where L_λ: is the TOA spectral radiance (Wm^{-2} sr^{-1} mm^{-1}), For Landsat 5 L_{max} =15.30; L_{min} =1.238.

2.4.3 Calculation of Brightness Temperature (BT)

Then, the temperature of satellite, Tb (in degrees Celsius), computed using the following Equation (4) after converting DN to radiance:

$$T_b = \frac{K_2}{\ln(\frac{K_1}{L_\lambda} + 1)} - 273.15$$

Equation 4

Where: The brightness temperature (Tb) is expressed in Celsius(°C), L_λ = is spectral radiance in (Wm^{-2} sr^{-1} mm^{-1}), K_1= from the metadata is specific thermal Band conversion constant equal 607.76, 774.89 for band 6 (Landsat 5) and 10 (Landsat 8) respectively, Band-specific thermal conversion K_2 equaled 1260.56, 1321.08 for band 6 (Landsat 5) and 10 (Landsat 8), respectively, based on metadata.

2.4.4 Calculation of NDVI

Normalized Difference Vegetation Index (NDVI) is determined by using the visible and near-infrared bands of Landsat as in Equation (5). The current quantity of vegetation is an important component, and NDVI used to determine total vegetation state, hence estimating the NDVI is critical.

NDVI must be calculated because the fractional vegetation (FV) must be estimated thereafter FV and NDVI are inextricably linked, and Emissivity (ε) must also be computed, which is related with FV.

$$\text{NDVI}=\frac{NIR-RED}{NIR+RED}$$

Equation 5

NIR, RED represents the pixel values of Near Infrared bands and Red bands. The Landsat RED and NIR bands, as well as the shapefile for the research region, are required for this phase.

2.4.5 Calculation of Fractional Vegetation (FV)

Fractional vegetation monitoring is the process of measuring the area covered by trees, branches, and leaves in relation to the overall vegetation area. We need NDVI data derived to determine FV in Equation (6), The data for NDVI max and NDVI min are taken from an NDVI raster image . The only input necessary in this stage is the NDVI raster dataset.

$$FV = (\frac{NDVI-NDVI_{min}}{NDVI_{max}-NDVI_{min}})^2$$

Equation 6

2.4.6 Calculation of Surface Emissivity (ε)

The ratio of emitted radiation from any surface to radiation from a blackbody of the same temperature is known as emissivity. Emissivity used to compute the thermal radiation from body of materials. For pixels which its NDVI is less 0.1 so the pixel is bare soil (no vegetation), emissivity is 0.96, when NDVI is more than 0.72 so the pixel is consider pure vegetation then ε_v is equal 0.985 and if NDVI is between 0.1 and 0.72 so the pixels are mixed pixel which mean ε is calculated according Equation (7) [38].

$$\begin{cases} NDVI < 0.1 & \varepsilon_s = 0.96 \\ 0.1 \le NDVI \le 0.72 & \varepsilon = \varepsilon_V FV + \varepsilon_S (1 - \text{FV}) + \text{d}_\varepsilon \\ NDVI > 0.72 & \varepsilon_v = 0.985 \end{cases}$$

Equation 7

where ε is land surface emissivity, ε_V is vegetation emissivity, ε_s is soil emissivity and d_ε refer to the surface roughness, that can be negligible for flat surfaces ($\text{d}_\varepsilon = 0$), though, for rough surfaces with value 2%, equation (8) can be applied to estimate it [39].

$$\text{d}_\varepsilon = (1 - \varepsilon_s)(1 - \text{Pv})\text{F}\varepsilon_V$$

Equation 8

Where F is Shape factor [39], considering various geometrical distributions,is 0.55[40]. Only one argument is required for this step: Dataset for Fractional Vegetation (FV).

2.4.7 Calculation of land surface temperature

Lastly, LST is calculated using the following Equation (9) [41]:

$$\text{LST} = \frac{T_b}{1+\left(\lambda*\frac{T_b}{\rho}\right)\ln(\varepsilon)}$$

Equation 9

LST indicates land surface temperature, and Tb is the brightness of sensor temperature. The wavelength of the radiance is given as λ and Ɛ identifies the land surface's spectral emissivity. Aside from, $\rho = c/\sigma = 1.438 \times 10^{-2}$ mk, where h equal to 6.626×10^{-34} Js which is Plank's constant, c equal to 2.998×10^{8} ms^{-2} indicate the velocity of light and $\sigma = (5.67 \times 10 - 8$ Wm^2 k$^{-4} = 1.38 \times 10^{-23}$ JK^{-1} is the Boltzmann constant. The final LST calculation interface requires Brightness Temperature dataset and emissivity dataset.

2.4.8 Estimation of Urban Heat Island (UHI)

The following methods were used to identify UHI and non-UHI zones [18].

$$\text{LST} > \mu + 0.5\sigma$$

Equation 10

$$0 < \text{LST} \le \mu + 0.5\sigma$$

Equation 11

The mean LST in the study area is μ and its standard deviation is σ. UHI zones are defined by Equation (10) as areas with LST greater than the sum of the mean of LST for each year and the half of standard deviation. UHI spots are the hottest parts of the city. The remainder of the city, outside the UHI, is categorized as non-UHI. Equation (11) In non-UHI areas, the ratio of water bodies and vegetation is higher, but in UHI areas, the predominant LU/LC categories are bare land and built-up areas.

2.4.9 Ecological Status Determination Using (UTFVI)

The Urban Thermal Field Variance Index (UTFVI), which is determined quantitatively by the UHI effect, takes into consideration the socioeconomic component. Equation (12) was used to compute the UTFVI [42].

$$\text{UTFVI}=\frac{T_s-T_{mean}}{T_{mean}}$$

Equation 12

UTFVI refer to the Urban Thermal Field Variance Index. T_s= LST for each year of study period (°C), Tmean = Mean LST (°C). Based on their UTFVI ratings, the study area was further divided into six different classes, as shown in Table 3 [43].

2.5 Validation of the Derived LST

Although well-established equations were used to obtain LST, there were some restrictions. Clear skies and images with less than 10% cloud over the study area are necessary for accurate LST estimation. Because there is some cloud cover over the research area, LST estimations may be overestimated or underestimated. Such issues could result in the incorrect estimation of historical, current, and forecast LST values in any location. Highest and lowest temperature data were collected from several Egyptian Meteorological Authority weather stations in the research area for 1991, 2001, 2011, and 2021 to validate the LST values using Landsat thermal data.

The difference between in situ LST and computed values can be more than 10°C [44]. Such a difference is mostly seen in urban areas where different features are randomly distributed. Thus, validating the computed data from satellite images is essential. A Z-test is used in hypothesis testing to evaluate whether a finding or association is statistically significant or not. In particular, it tests whether two means are the same (the null hypothesis) or not. The Z-test can only be used if the population standard deviation is known and the sample size is 30 data points or larger Equation (13):

$$Z = \frac{X-\mu}{\sigma}$$

Equation 13

where X refers to the mean value of ground-measured temperature, μ refers to the mean value of the derived LST, and σ indicates the standard deviation of LST values.

2.6 Simulation of LST and LU/LC Using CA-ANN Algorithm

Forecasting the LU/LC and LST distribution over the coming decade is an important part of the study. The spatiotemporal distribution of LST and LU/LC is predicted using multiple models, including ANN, CA, MC, and regression approaches [45]. For this study, the MOLUSCE plugin tool in QGIS software was applied to forecast the 2031 LST and LU/LC distribution, which is regarded as one of the finest prediction models [46]. MOLUSCE is a software tool that analyses, displays, and simulates changes. It employs standard techniques such as CA, ANN, Weights of Evidence, Multi-Criteria Evaluation, and Logistic Regression [47]. MOLUSCE is extremely user-friendly and has a wide range of modules and capabilities. The plugin is made up of several components, including an input module, a trend analysis, modelling techniques, prediction, and validation [48]. The area changes analysis LU/LC and LST changes between two time periods, creates transition matrices, and maps the LST and LU/LC change distribution maps. In the modelling approaches stage, the ANN model is applied to forecast LST and LU/LC transaction potential.

After a few trials, 6 hidden layers with 1-3n hidden neurons in each layer were chosen for LST and LU/LC prediction. Here, 3 is the number of time series layers at 10-year intervals, and n is 8 LST and LU/LC, depending on the input layers used in Equation (14,15), with the maximum iteration set at 1000. Using a neural network, transition potentials predict the likelihood of future LU/LC and LST changes and reveal the descriptive power of driving factors. The neighborhood pixel was set to 9 cells (3 x 3) to generate the model's maximum iterations and pixels. A series of previous years LST, LU/LC maps, NDBI, NDBSI pictures at intervals of 10 and 20 years, latitude and longitude were provided as input parameters to the ANN model to find hidden patterns within the datasets and create the prediction by moving along the data from time series for LST prediction [49], [50].

Table 3: The Range and classes of UTFVI

UTFVI	UHI phenomenon	Ecological Evaluation Index
<0.000	None	Excellent
0.000–0.005	Weak	good
0.005–0.010	Middle	normal
0.010–0.015	Strong	Bad
0.015–0.020	Stronger	Worse
>0.020	Strongest	Worst

The same process was followed to predict the LU/LC with 10 and 20 years' interval data of LU/LC, Distance from road (DFR), slope and Digital Elevation Model (DEM), latitude, and longitude act as the inputs parameters. The LST and LU/LC predicted output for the next 10 (t+10) and 20 (t+20) years, shown mathematically in Equation (14,15):

$$LST(t+10) = f\begin{bmatrix} LST(t), LST(t-10), \frac{LU}{LC}(t), \\ \frac{LU}{LC}(t-10), NDBI(t), NDBI(t-10), \\ NDBSI(t), NDBSI(t-10) \end{bmatrix}$$

Equation 14

As, t = 2021

$$\frac{LU}{LC}(t+10) = f\begin{bmatrix} LST(t), LST(t-10), DFR(t), \\ DFR(t-10), DEM(t), DEM(t-10), \\ Slope(t), Slope(t-10) \end{bmatrix}$$

Equation 15

As, t = 2021

3. Result and Discussion

3.1 Analysis of LU/LC Classification Changes

The SVM technique extracted the changing trends in LU/LC classes from Landsat data between 1991 and 2021. The classification accuracy of the classified LU/LC maps was evaluated using kappa statistics, user accuracy, producer accuracy, and overall classification accuracy. As presented in Table 4, the overall classification accuracies for 1991, 2001, 2011, and 2021 were 94%, 93.5%, 95.25%, and 93.73%, respectively, indicating a high level of agreement.

In 1991, most of the land was covered by vegetation, 79.36%, whereas 15.47% was built up. Then, the water body (4.62%) was followed by the bare land (0.55%). After ten years, in 2001, the amount of built-up area increased to 26.54%, and the vegetation percentage decreased to 72.45%. In 2011, the built-up area increased to 33.31%. As a result, vegetation and bare soil decreased to 64.78% and 0.06%, respectively. In 2021, the built-up area and bare land ultimately increased to 41.83% and 0.9%, respectively, whereas vegetation and water bodies were reduced to 55.83% and 1.43%, respectively. From 1991 to 2021, the percentages of the built-up area increased by 26.36%, whereas the green area and water bodies decreased by 26.72%. Thus, it can be deduced that the built-up area occupies a reduced area of vegetation and water bodies. As presented in Table 5, the above statistics indicate that the amount of greenery, bare soil, and waterbodies decreased as the built-up region grew. These changes may also be expressed visually by these land cover types using the time series data in Figure 2. It shows that the amount of built-up area increases over time, making the region redder (as the built-up area is shown in red). In contrast, various land coverings decline with time.

Unplanned urban expansion to accommodate the growing urban population, unregulated rural-to-urban migration, and haphazard infrastructure development are potential reasons for these changes. The fundamental theory showed that this substantial urban growth involves strategic and economic concerns, resulting in a decline in natural resources and characteristics like vegetation cover and water bodies [51].

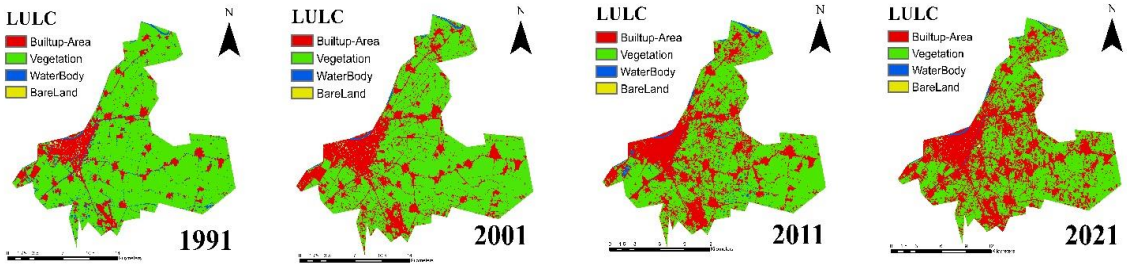

Figure 2: LU/LC classification using SVM over Mansoura city from 1991 to 2021

Table 4: LU/LC Classification using SVM accuracy assessment

	User Accuracy				Producer Accuracy				Overall Classification Accuracy	Overall Kappa Statistics
	Built-up	Vegetation	Water Bodies	Bare Land	Built-up	Vegetation	Water Bodies	Bare Land		
1991	92.45	96.17	91.78	92.11	92.45	94.12	100.00	87.50	94.0%	0.9112
2001	94.70	94.79	94.92	80.65	91.74	96.81	91.80	83.33	93.5%	0.9010
2011	95.90	96.61	91.53	92.86	96.70	95.53	94.74	90.77	95.25%	0.9299
2021	94.48	96.07	90.00	86.36	93.75	96.07	93.75	84.44	93.73%	0.9067

Table 5: Distribution of various LU/LC classes over Mansoura city from 1991 to 2021

	1991		2001		2011		2021	
LU/LC (Area)	(Km^2)	%	(Km^2)	%	(Km^2)	%	(Km^2)	%
Built-up	49.83	15.47	85.51	26.54	107.29	33.31	134.75	41.83
vegetation	255.65	79.36	233.39	72.45	208.69	64.78	179.86	55.83
water body	14.89	4.62	2.21	0.69	5.97	1.85	4.62	1.43
Bare Land	1.76	0.55	1.02	0.32	0.18	0.06	2.90	0.9

Table 6: Validation of estimated land surface temperature using weather station data for Mansoura city

Year	**1991**		**2001**		**2011**		**2021**	
	Max	Min	Max	Min	Max	Min	Max	Min
Remote Sensing LST	38.38	24.11	43.33	24.97	44.08	25.82	45.03	27.16
Ground measurements	37.33	22.61	41.61	24.39	41.50	26.22	42.89	24.78
Difference	-1.05	-1.50	-1.72	-0.58	**-2.58**	**0.40**	-2.14	-2.38
Average Difference	-1.27		-1.15		-1.09		-2.26	

Table 7: Z-test results

	1991	**2001**	**2011**	**2021**
Mean LST (μ)	27.363473	29.15262	30.45797	33.20083
SD (σ)	2.2289936	3.184438	2.73752	2.596085
Mean temperature collected from ground station (X)	29.97	33	33.86	33.835
Z-Score	1.1693738	1.208182	1.242741	0.244279
p-value two tailed test	0.242	0.226	0.213	0.807
Position on normal distribution curve	Located at "Random area"			

3.2 LST Change Variation Across Mansoura City

3.2.1 Validation of the derived LST

At about 2m above the ground in an open field, weather stations operated by the Egyptian Meteorological Authority recorded the temperature, as shown in Table 6. The difference was calculated between the ground measurements and derived LST. A negative difference (ND) indicates that the estimated LST value is more than the ground recorded temperature, whereas a positive difference (PD) is vice versa. The lowest PD (0.4) and highest ND (-2.58) were found in 2011.

Considering all the constraints of remote sensing derived LST data, the difference between the estimated LST and measured temperature was minor and determined to be satisfactory, which could be used for further study. To validate the estimated LST values obtained from Landsat thermal data, the lowest and highest temperature data were collected from weather stations for 1991, 2001, 2011, and 2021 in the study region Table 6. The statistical difference between LST and ground measurements was tested using a Z-score. It tested whether the LST and ground measurement means were identical. Table 7 shows the Z-score and the corresponding p-value, which confirms no significant difference between ground measurements and LST. Also pearson correlation Pearson's correlation between mean LST derived from satellite data and mean temperature collected from ground station across study period is shown in Figure 3.

3.2.2 Changes in LST range classes over Mansoura city

Table 8 illustrates the LST's mean and standard deviation used to calculate the threshold LST value for UHI and non-UHI spots. The annual distribution of LST from 1991 to 2021 exhibits rising trends. The highest recorded temperature in 1991 was 38.39°C, which was greater than before considerably in 2021 to 45.03°C with a 0.22°C yearly change. Additionally, the lowermost temperature ever recorded was 24.11°C in 1991, which increased significantly by 27.16°C in 2021, with a rise of 0.1°C every year, correspondingly. As shown in Figure 4 and Table 9, temperatures above 25°C were observed in 67.17% (216.36 km^2) of the study area in 1991. Additionally, in 1991, 19.31% of the study area was in the 25°C–30°C temperature range, which increased to 52.14% in 2011. Moreover, in 1991, 13.53% of the study area was in the 30°C–35°C temperature range, which increased to 67.72% in 2021.

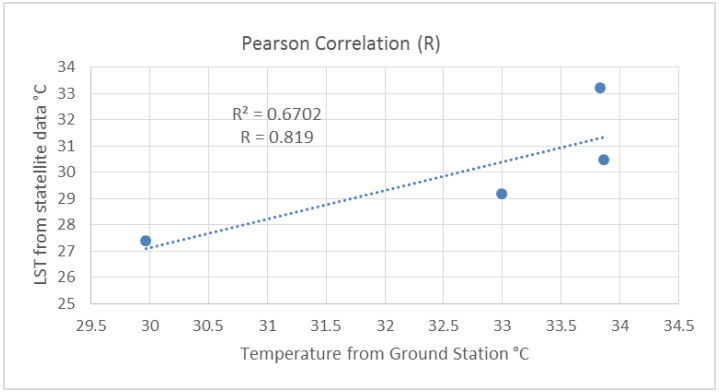

Figure 3: Pearson correlation between LST and ground stations temperatures

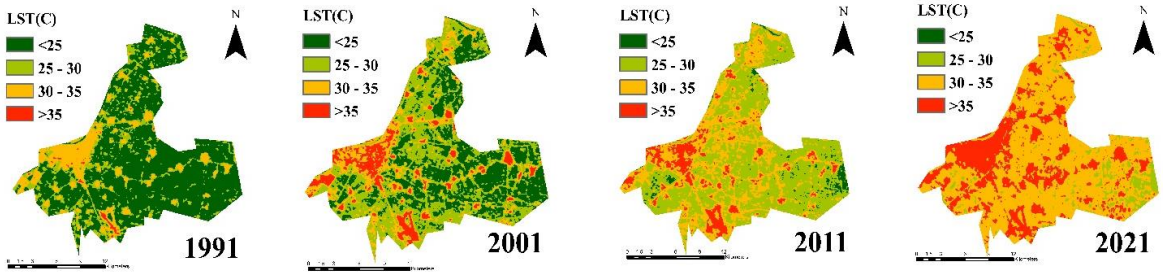

Figure 4: LST maps for Mansoura city in 1991, 2001, 2011, and 2021

Table 8: Retrieved statistics of LST (°C) values in Mansoura city (1991–2021)

	Mean	STD	Threshold LST value for UHI
1991	27.36	2.23	28.48
2001	29.16	3.18	30.75
2011	30.46	2.74	31.83
2021	33.20	2.60	34.50

Table 9: Distribution of LST over Mansoura city from 1991 to 2021

	Range of LST (◦C)							
	<25		25-30		30-35		>45	
Area	**km^2**	**%**	**km^2**	**%**	**km^2**	**%**	**km^2**	**%**
1991	216.36	67.17	60.20	19.31	43.57	13.53	0	0
2001	107.80	33.47	129.58	40.23	56.31	17.48	28.44	8.83
2011	8.65	2.68	167.94	52.14	116.31	36.11	29.22	9.07
2021	0	0	19.99	6.20	218.16	67.72	83.96	26.06

Therefore, the surface temperature of the study area is expected to rise significantly under this scenario, even though no area and 8.83% of the area had a high temperature in 1991 and 2001, respectively, and the area forced the highest temperature in 2021 increase to 26.06% of the study area. If the current trend continues, it will expand substantially in the next few years.

According to the LST variance in different LU/LC classes, the water body and vegetation area were observed as a lower temperature zone from 1991 to 2021 because of reduced heat absorption and transpiration. In particular, the urban area and bare land are recorded as the highest temperature zone due to their hard surfaces and naturally sunlight-reflecting character. Buildings in urban areas emit long thermal infrared waves and significant heat radiation, which enhance LST [52], [53]. The progressive increase in LST leads to a rise in UHI. The LST changes over various LU/LC class statistics provide a more detailed knowledge of UHI effects in the urban region by removing the green cover and replacing it with a hardscape.

3.2.3 Distribution of LST for each LU/LC class

The mean LST of each LU/LC class is the same as the time series in Figure 5. The LST for water bodies was 28.20°C in 1991 and increased to 32.21°C in 2021. Meanwhile, the LST for bare land was 31.86°C in 1991 and increased to 36.69°C in 2021. The LST for vegetation was around 26.48°C in 1991 and increased to 31.66°C in 2021. The LST for built-up regions was around 31.46°C in 1991 and will increase to 35.30°C in 2021. Over time, built-up areas and bare land remained warmer than the mean LST, whereas water bodies and vegetation remained cooler. The vegetation had the lowest LST of the LU/LC classes, which aids in keeping the LST of the area low. Bare land had the highest LST across all years.

3.3 Relationship between LU/LC Indices and LST

Figure 6 shows the spatial distribution of LU/LC indices (NDVI, NDBI, NDWI, and NDBSI). The relationship between LST and LU/LC indices (NDVI, NDBI, NDWI, and NDBSI) was investigated using Pearson's correlation at significance level 95% (p-value < 0.05). The fishnet tool in ArcGIS 10.5 was used to retrieve values from LST and LU/LC indices (NDBI, NDVI, NDWI, and NDBSI) raster data and create points. Significant changes have been made yearly in the strength of the relationship between LU/LC indices and LST. Correlation coefficient values were significant at 0.05 level. According to the statistics, NDVI and LST are negatively correlated, whereas NDBI, NDWI, and NDBSI are positively correlated. Table 10 shows the relationship between the LST and LU indices over the research period. NDVI had a weak correlation with LST, whereas NDBI had a moderate correlation with LST. Among other indices, it had the second strongest correlation. NDBSI had the strongest correlation with LST of all land surface indicators. Moreover, NDWI and LST showed a positive correlation. The correlation between NDWI and LST was found to be positive in the study area. This could be due to that the percentage of surface water area in Mansoura city is very small. Some previous studies reported similar results that the LST relation with NDWI is positive correlated in all seasons expect winter season [54] [55] [56].

The linear regression model was used to investigate the impact of land surface indices on LST fluctuation. Each model used one land surface index as the independent variable and LST as the dependent variable [33]. R^2 and p-values were shown to interpret the outcomes. Figure 7 shows the model's results and the regression analysis equation. It has been found that all indicators significantly influence LST. In 1991, NDBI and NDBSI might explain approximately 80% and 81% of the growth in LST, respectively; although NDVI might explain a 63% decrease in LST. In 2001, NDBI and NDBSI accounted for 82% and 85% of the increase in LST, respectively, whereas NDVI accounted for 68% of the cooling in LST. Therefore, NDBI and NDBSI could explain approximately 80% and 81% of the increase in LST, respectively; although NDVI could contribute to a 66% decrease in LST in 2011. Moreover, NDBI and NDBSI might explain approximately 80% and 81% of the growth in LST, respectively.

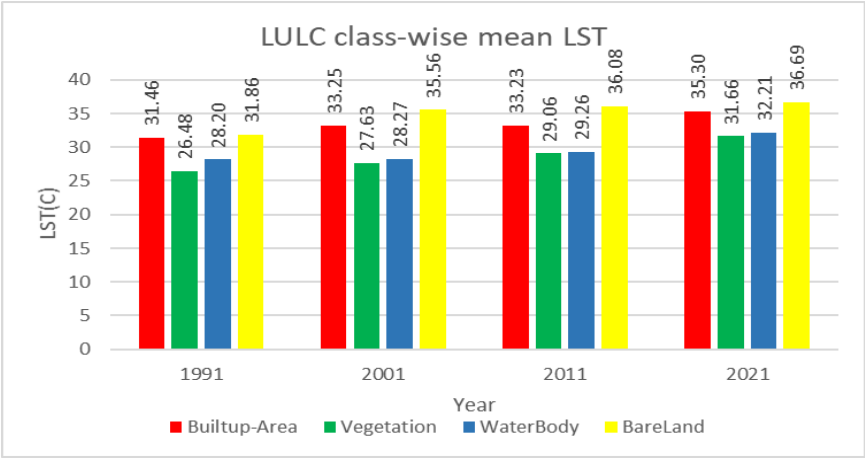

Figure 5: Mean LST by LU/LC over the year

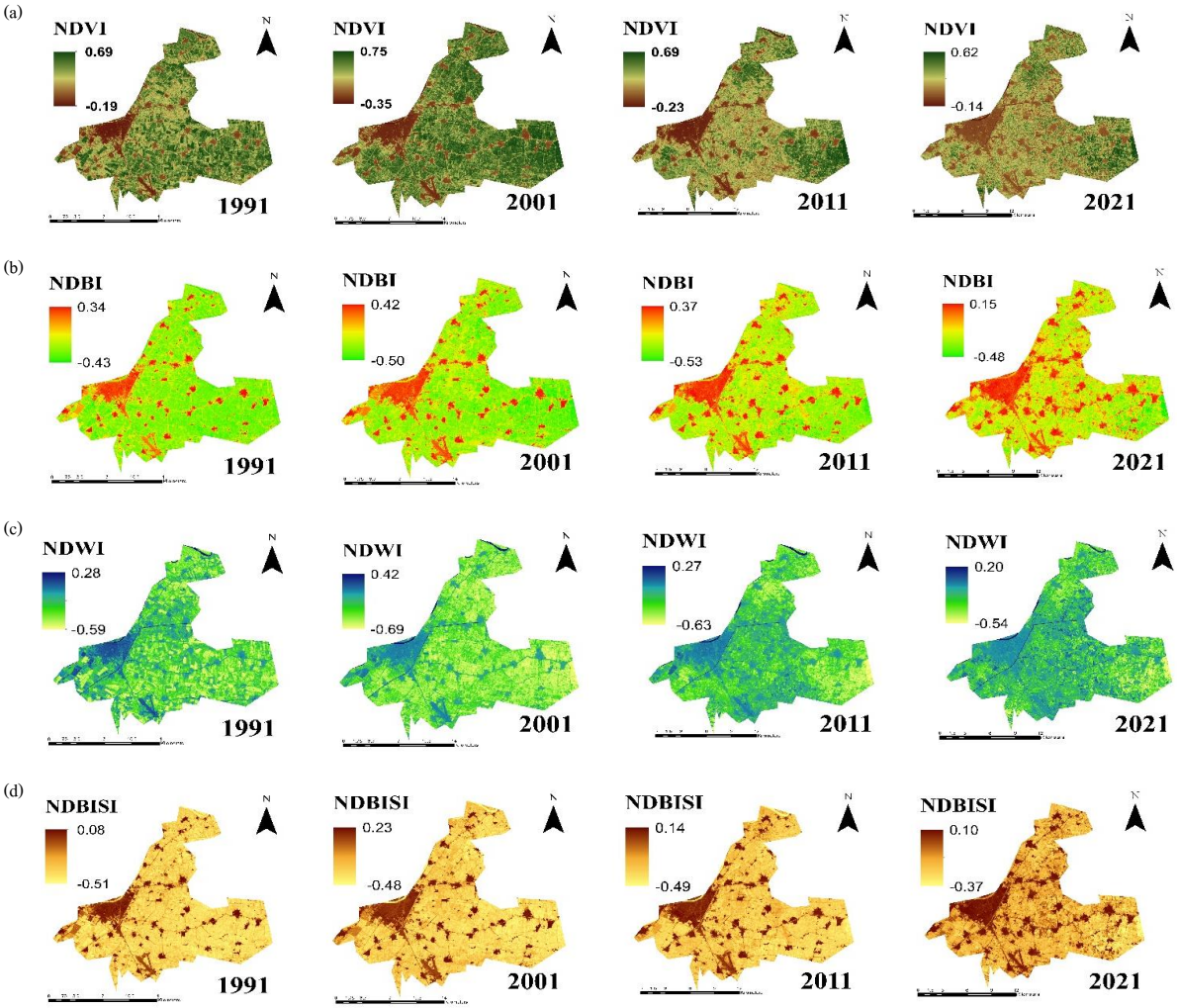

Figure 6: Variation of LU/LC indices (a) NDVI; (b) NDBI; (c) NDWI; (d) NDBSI in Mansoura city in 1991, 2001, 2011, and 2021

Table 10: Correlation matrix between LST and different land surface indices

1991					
	LST	NDVI	NDBI	NDWI	NDBSI
LST	1				
NDVI	-0.74	1			
NDBI	0.89	-0.82	1		
NDWI	0.59	-0.97	0.68	1	
NDBSI	0.90	-0.72	0.97	0.54	1
2001					
	LST	NDVI	NDBI	NDWI	NDBSI
LST	1				
NDVI	-0.83	1			
NDBI	0.90	-0.89	1		
NDWI	0.74	-0.98	0.82	1	
NDBSI	0.90	-0.83	0.98	0.73	1
2011					
	LST	NDVI	NDBI	NDWI	NDBSI
LST	1				
NDVI	-0.75	1			
NDBI	0.86	-0.73	1		
NDWI	0.59	-0.96	0.56	1	
NDBSI	0.87	-0.70	0.99	0.50	1
2021					
	LST	NDVI	NDBI	NDWI	NDBSI
LST	1				
NDVI	-0.49	1			
NDBI	0.67	-0.76	1		
NDWI	0.42	-0.99	0.70	1	
NDBSI	0.72	-0.80	0.98	0.74	1

Table 11: Variations of LST in UHI and non-UH spots

	LST (MIN)		**LST (MAX)**		**LST (Mean)**		**LST (STD)**	
	UHI	Non-UHI	UHI	Non-UHI	UHI	Non-UHI	UHI	Non-UHI
1991	28.768	24.115	38.389	28.352	31.218	26.406	1.834	0.871
2001	30.830	24.974	43.337	30.420	34.417	27.656	2.383	1.138
2011	32.051	25.827	44.083	31.645	34.875	29.196	2.091	1.104
2021	34.499	27.164	45.033	34.499	36.558	31.763	1.489	1.335

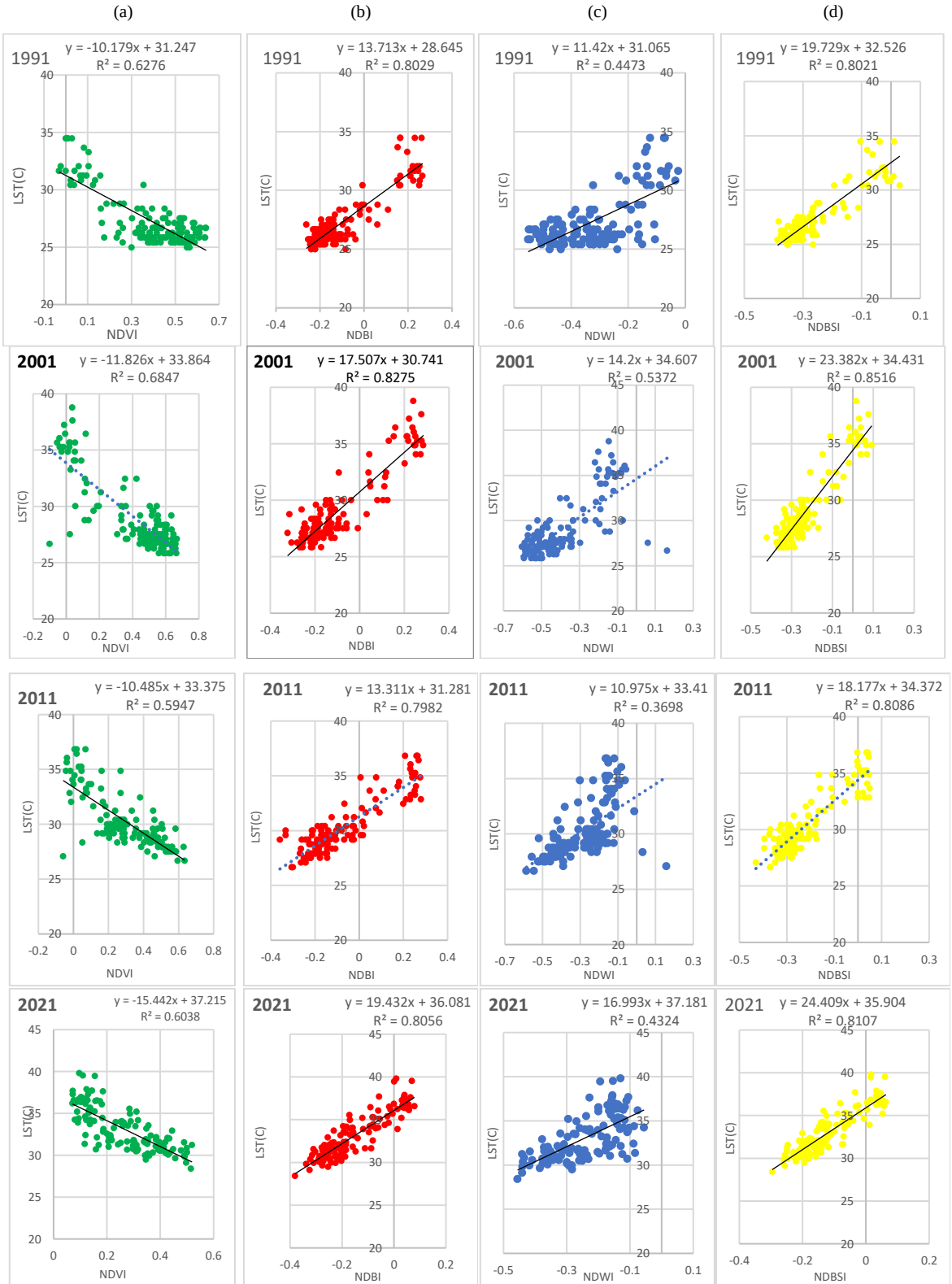

Figure 7: Linear regression analysis between LST and LU/LC indices (a) NDVI; (b) NDBI; (c) NDWI; (d) NDBSI

3.4 UHI and Non-UHI Spots

The strength of UHI was determined by comparing the mean LST values in UHI and non-UHI. Table 11 shows that in 1991, 2001, 2011, and 2021 UHI spot maps, the difference between the mean LST values for UHI and non-UHI spots is 4.72°C, 4.95°C, 4.47°C, and 4.38°C, respectively. The mean value of LST on the UHI and non-UHI spots increased by more than 5°C from 1991 to 2021 which indicate the intensity of UHI increase over the study period. The major built-up regions and undeveloped territory inside the city boundaries were indicated as the UHI zones on all maps. The common UHI zones were established mainly in the city's north-west sector (bare lands and built-up regions), as shown in Figure 8. A Kolmogorov–Smirnov test was conducted to explore the normality of LST data. The results showed that LST was not normally distributed, as shown in Table 12 and Figure 9. These results indicate that a nonparametric test should be applied to test the difference between UHI and non-UHI spots. Moreover, Mann–Whitney U test showed that LST values had a significant difference across UHI and non-UHI zones (p-value < 0.005) at a significant level of 0.05. The data were analyzed using IBM SPSS statistics.

3.5 Ecological and Thermal Status Using UTFVI

UTFVI designates the level of thermal comfort in the environment as the benchmark of urban health and ecology [9]. Figure 11 shows the UTFVI distribution threshold values for 1991, 2001, 2011, and 2021. Table 13 shows the distribution of UTFVI's area. In 1991, 67.17% of the area had no UTFVI effect, which decreased to 58% in 2021, despite the highest value of UTFVI being 2.44%, 4.83%, 3.34%, and 3.61% in 1991, 2001, 2011, and 2021, respectively. The UTFVI distribution illustrates that none and weak UTFVI zones have substantially reduced throughout the years across Mansoura city, whereas strong, stronger, and strongest regions have significantly grown. The best thermal conditions for a living are none and have a weak influence on UTFVI, whereas the strongest zone indicates a vulnerable environment susceptible to larger UHI phenomena. The findings of the UTFVI research consequently underline the city's ongoing deterioration in habitability.

3.6 Prediction of LU/LC and LST

3.6.1 Validation of LU/LC and LST scenario prediction

The LU/LC and LST for 2021 were initially predicted using the CA-ANN model for validating the prediction data's accuracy. Table 14 shows the comparison results between the predicted and estimated maps using various kappa coefficients and QGIS-MOLUSCE Plugin. K-location, K-no, K-location Strata, and K-standard performed well, with values of 0.89, 0.87, 0.9, and 0.88, respectively. The percentages of correctness and overall kappa were 88.77 and 0.81, respectively (Table 14).

3.6.2 Prediction of LU/LC changes

The predicted LU/LC maps revealed a considerable rise in a built-up area and a decrease in green and bare land and water areas cover. Changes in LU/LC results are presented in Table 15. In the predicted year (2031), 20.2% of the land will be converted to built-up areas compared to 2021. Meanwhile, in 2031, the vegetation cover will fall by −18.74%.

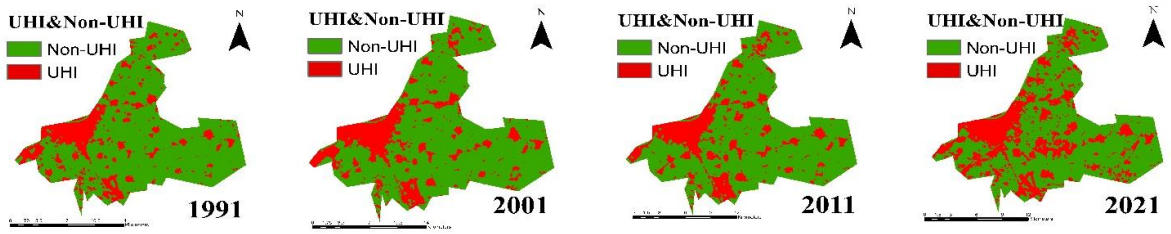

Figure 8: UHI and non-UHI spots of Mansoura city

Table 12: Test of normality by Kolmogorov–Smirnov test for LST in 1991, 2001, 2011, and 2021

	Kolmogorov-Smirnova		
	Statistic	*df*	Sig.
LST 1991	.247	136	.000
LST 2001	0.225	135	.000
LST 2011	0.210	133	.000
LST 2021	0.138	135	.000

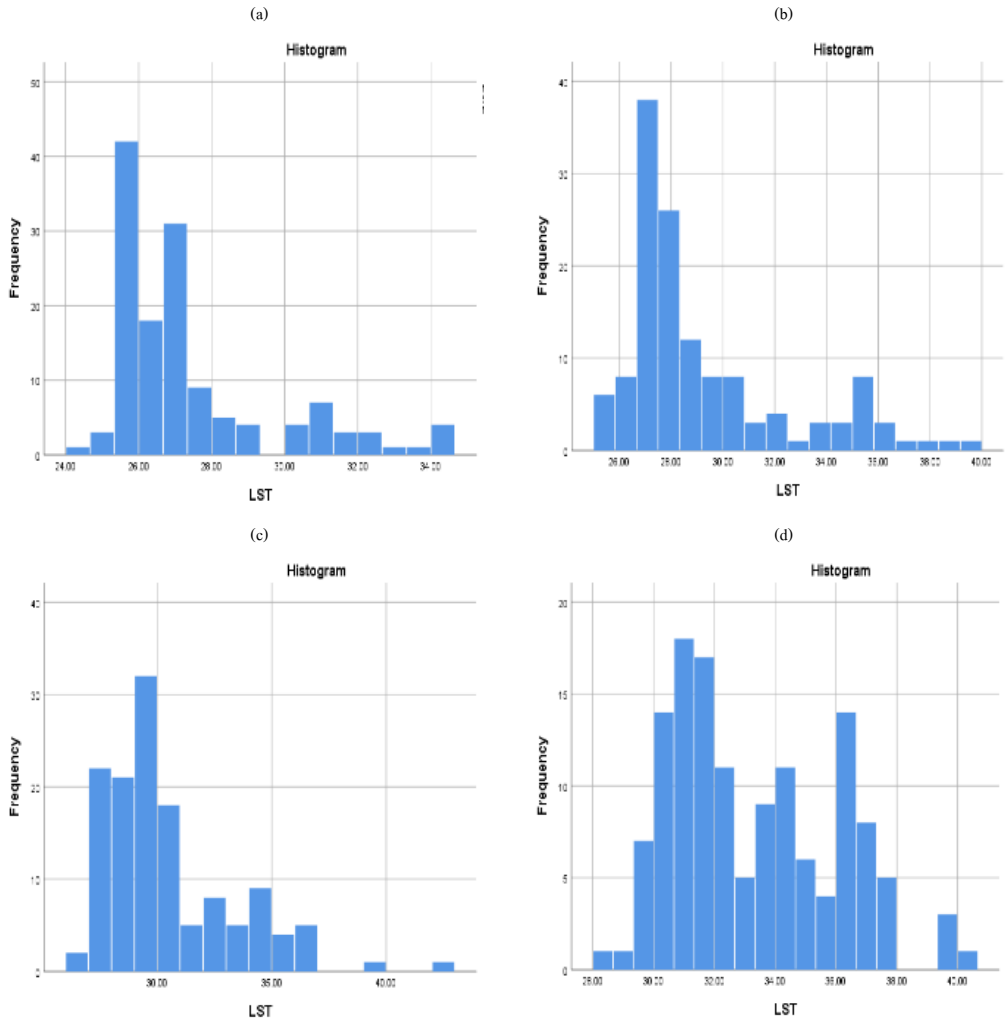

Figure 9: Distribution of LST data in (a) 1991, (b) 2001, (c) 2011, and (d)2021

Table 13: Distribution of UTFVI's area (%) in Mansoura city from 1991 to 2021

Year	Class Range	<0	0-0.005	0.005-0.01	0.01-0.015	0.015-0.02	>0.02
	Class Name	None	Weak	Middle	Strong	Stronger	Strongest
1991	Area (%)	67.17	15.31	4.70	5.63	4.76	2.44
2001	Area (%)	66.49	11.38	5.19	6.96	5.15	4.83
2011	Area (%)	69.44	8.34	5.90	7.25	5.73	3.34
2021	Area (%)	58.00	7.84	12.66	10.53	7.37	3.61

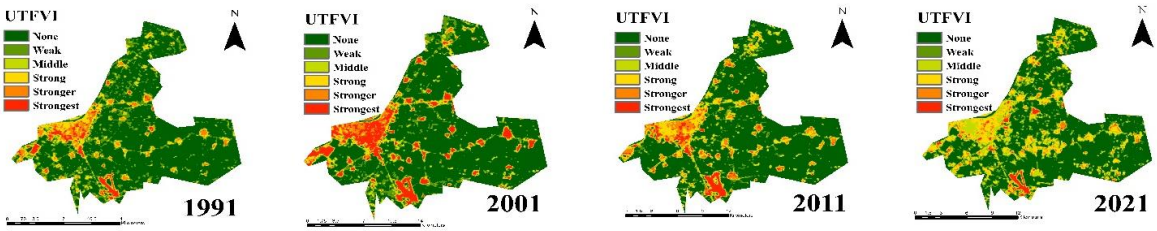

Figure 10: Ecological evaluation index of Mansoura city according to UTFVI

Table 14: CA-ANN model validation of the LU/LC simulation image for 2021

Prediction Year	Validation of the CA-ANN model for predicted LU/LC					
	QGIS-MOLUSCE Plugin Module Kappa Parameters					
	K-location	K-no	K-location Strata	K-standard	%-correctness	Overall Kappa Value
LU/LC 2021	0.89	0.87	0.9	0.88	88.77	0.81
	Validation of the CA-ANN model for predicted LST					
LST 2021	0.85	0.89	0.91	0.85	83.36	0.79

Table 15 Changes in LU/LC in Mansoura city predicted for 2031

LU/LC Classes	1991		2001		2011		2021		2031		Overall Change %	
	Area	%	Area	%	Area	%	Area	%	Area	%	2021-2031	1991-2031
Built-up Area	49.83	15.47	85.51	26.54	107.29	33.31	134.75	41.83	199.83	62.03	20.20	46.57
Vegetation	255.65	79.36	233.39	72.45	208.69	64.78	179.86	55.83	119.496	37.10	-18.74	-42.27
Water Body	14.89	4.62	2.21	0.69	5.97	1.85	4.62	1.43	2.0718	0.64	-0.79	-3.98
Bare Land	1.76	0.55	1.02	0.32	0.18	0.06	2.90	0.90	0.7326	0.23	-0.67	-0.32

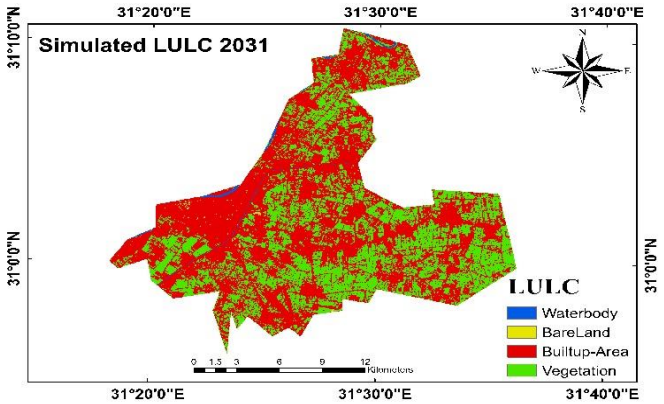

Figure 11: Predicted LU/LC map for 2031

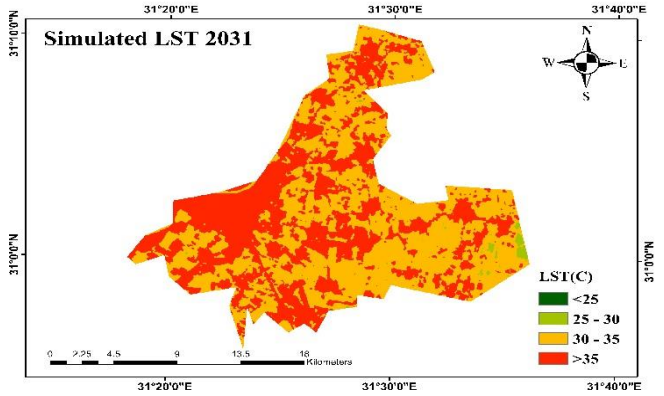

Figure 12: Predicted LST map for 2031

Furthermore, the change in a built-up area in the study period from 1991 to the predicted year (2031, 40 years) decreased by 46.57%, whereas the vegetation areas decreased by 42.27%, Figure 11.Urban health, ecological services, and thermal characteristics of the city may be impacted by decreases in vegetation cover and rises in urban areas created by displacing green cover.

The effects of UHI and UTFVI will intensify if the current urbanization trend continues, creating a plethora of health, economic, and environmental problems in the research area. Reducing the impacts of UHI and UTFVI, proper land planning, the protection of water bodies, and an expansion in urban green space will help to make Mansoura city more sustainable.

3.6.3 Prediction of LST for 2031

The predicted scenario suggested that higher temperate areas will most likely occur in the southwestern region, primarily built-up. Figure 12 shows future anticipated LST maps and range-wise LST variability. Moreover, LST in 2031 increased significantly because the projection was based on historical LST distribution patterns. In the summer, the sun's rays strike the ground at a sharp angle, influencing the increase in temperature with a massive increase in impervious layers. In summer 2031, half of the study region (54.97%) would suffer LST in the range of 30°C–35°C, followed by 44.30% in the range of <45°C compared to only 26.06% of the study area faced this range in 2021. In 2031, only 0.73% of the land will be recorded in the 25°C–30°C temperature zone range.

4. Conclusion

The research is being conducted to develop a user-friendly Python tool that can calculate LST and UHI data in less time for Landsat. Since 1991, the total urban area has expanded by more than 24%, resulting in a decline in vegetation (19%) and water bodies (5.7%). Mean LST increased by about 5.84°C in the last thirty years, and 67.72% of the total area faced 30°C–35°C temperatures in 2021; however, it was only 13.53% of the total area in 1991.

The UHI area, which is severe under heat stress, increased from 64.095 km^2 (19.9%) of the total area of Mansoura city to 96.58 km^2 (29.98%) from 1991 to 2021. It is worth noting that increasing urbanization is a significant factor in LU/LC and LST variations and the consequent rise of UTFVI. In 2021, 10.53% of the study area was exposed to a strong UTFVI effect, compared with only 5.63% in 1991. According to an upcoming LU/LC study, vegetation and water body areas will decline by 42.27% and 3.98%, respectively, in 2031, compared with 1999. Future LST predictions imply that 26% of the overall area would likely encounter temperatures above 45°C in 2031. However, in 1999, no area of Mansoura city experienced this temperature. If this trend remains, the city's built-up regions and LST will continue to develop over the next decade, causing a slew of medical, economic, and environmental issues. The findings of the study will be helpful to politicians, policymakers, government representatives, and urban planners in Mansoura city, who will be able to utilize the study's financing for future planning and decision-making. To make sure that other Egyptian cities expand sustainably, it is essential to investigate and model urban growth, changes in LU/LC, and LST distribution.

In the future, several more researches may be conducted. First, research may be conducted using various satellite data with various temporal and spatial resolutions, such as Quick bird (0.6 m), ASTER (15 m), IKONOS (1 m), MODIS (1000 m), and Sentinel-2A (10 m). Second, variations in the correlation coefficients between the LST and LULC indices may be analyzed over a more extended time and in other seasons (winter, fall, or spring). Third, different LULC indices (e.g., combined vegetation index, bare soil index, land surface water index, and urban index) may be investigated to see which has the best correlation with LST. Furthermore, we may conduct this research in several environments with different physical features. Finally, other machine learning algorithms (e.g., residual neural networks, AlexNet, and GoogLeNet) may be used to predict LU/LC and LST.

References

[1] Artuso, F. and Guijt, I., (2020). *Global Megatrends: Mapping the Forces that Affect us all*. http://hdl.handle.net/10546/620942

[2] Kleemann, J., Baysal, G., Bulley, H. N. N. and Fürst, C., (2017). Assessing Driving Forces of Land Use and Land Cover Change by a Mixed-Method Approach in North-Eastern Ghana, West Africa. *J. Environ. Manage.*, Vol. 196, 411–442. https://doi.org/10.1016/j. jenvman.2017.01.053

[3] Bratley, K. and Ghoneim, E., (2018). Modeling Urban Encroachment on the Agricultural Land of the Eastern Nile Delta Using Remote Sensing and a GIS-Based Markov Chain Model. *Land*, Vol. 7(4). https://doi.org/10.3390/land7040114

[4] Abu Hatab, A., Cavinato, M. E. R., Lindemer, A. and Lagerkvist, C. J., (2019). Urban Sprawl, Food Security and Agricultural Systems in Developing Countries: A Systematic Review of the Literature. *Cities*, Vol. 94, 129–142. https://doi.org/10.1016/j.cities.2019.06.001

[5] Sonnino, R., (2016). The New Geography of Food Security: Exploring the Potential of Urban Food Strategies. *Geogr. J.*, Vol. 182(2), 190–200. https://doi.org/10.1111/geoj.12129

[6] Bokaie, M., Zarkesh, M. K., Arasteh, P. D. and Hosseini, A., (2016). Assessment of Urban Heat Island based on the Relationship between Land Surface Temperature and Land Use/ Land Cover in Tehran. *Sustain. Cities Soc.*, Vol. 23, 94–104. https://doi.org/10.1016/j.scs. 2016.03.009

[7] El-Hattab, M., Amany, S. M. and Lamia, G. E., Monitoring and Assessment of Urban Heat Islands over the Southern Region of Cairo Governorate, Egypt. *Egypt. J. Remote Sens. Sp. Sci.*, Vol. 21(3), 311–323. https://doi.org/10.1016/j.ejrs.2017.08.008

[8] Kafy, A. A., Saha, M., Faisal, A. A., Rahaman, Z. A., Rahman, M.T., Liu, D., Fattah, M. A., Rakib, A. A., AlDousari, A. E., Rahaman, Sk. N., Hasan, M. Z. and Ahasan, M. K. K., (2022). Predicting the Impacts of Land Use/Land Cover Changes on Seasonal Urban Thermal Characteristics Using Machine Learning Algorithms. *Build. Environ.*, Vol. 217. https://doi.org/10.1016/j.buildenv.2022. 109066

[9] Najafzadeh, F., Mohammadzadeh, A., Ghorbanian, A. and Jamali, S., (2021). Spatial and Temporal Analysis of Surface Urban Heat Island and Thermal Comfort Using Landsat Satellite Images between 1989 and 2019: A Case Study in Tehran. *Remote Sens.*, Vol. 13(21). https://doi.org/10.3390/rs13214469

[10] Vapnik, V. N. and Chervonenkis, A. Y., (2015). On the Uniform Convergence of Relative Frequencies of Events to their Probabilities. *Measures of Complexity*, Springer, 11–30.

[11] Vapnik, V. N., (1999). An Overview of Statistical Learning Theory. *IEEE Trans. Neural Networks*, Vol. 10(5), 988–999.

[12] Xiang, Y., Huang, C., Huang, X., Zhou, Z. and Wang, X., (2021). Seasonal Variations of the Dominant Factors for Spatial Heterogeneity and Time Inconsistency of Land Surface Temperature in an Urban Agglomeration of Central China. *Sustain. Cities Soc.*, Vol. 75. https://doi.org/10.1016/j. scs.2021.103285

[13] Yousef, S., Tazeh, M., Mirzaee, S., Moradi, H. R. and Tavangar, S. H., (2014). Comparison of Different Classification Algorithms in Satellite Imagery to Produce Land Use Maps (Case study: Noor city). Journal of RS and GIS for Natural, Vol. 5(3), 67-76. https://girs.bushehr.iau.ir/article_516 650.html?lang=en

[14] Walawender, J. P., Hajto, M. J. and Iwaniuk, P., (2012). A New ArcGIS Toolset for Automated Mapping of Land Surface Temperature with the Use of LANDSAT Satellite Data. *2012 IEEE International Geoscience and Remote Sensing Symposium*, 4371–4374.

[15] Guha, S., Govil, H., Gill, N. and Dey, A., (2020). Analytical Study on the Relationship between Land Surface Temperature and Land Use/Land Cover Indices. *Ann. GIS*, Vol. 26(2), 201–216, https://doi.org/10.1080/19475683. 2020.1754291

[16] Piyoosh, A. K. and S. K. Ghosh, (2022). Analysis of Land Use Land Cover Change Using a New and Existing Spectral Indices and its Impact on Normalized Land Surface Temperature. *Geocarto Int.*, Vol. 37(8), 2137–2159.

[17] Guha, S. and Govil, H., (2021). COVID-19 lockdown Effect on Land Surface Temperature and Normalized Difference Vegetation Index, *Geomatics, Nat. Hazards Risk*, Vol. 12(1), 1082–1100. https://doi.org/10.1080/19475705. 2021.1914197

[18] Guha, S., Govil, H., Dey, A. and Gill, N., (2018). Analytical Study of Land Surface Temperature with NDVI and NDBI using Landsat 8 OLI and TIRS Data in Florence and Naples City, Italy. *Eur. J. Remote Sens.*, Vol. 51(1). 667–678.https://doi.org/10.1080/227972 54.2018.1474494.

[19] Guha, S., (2021). Dynamic Seasonal Analysis on LST-NDVI Relationship and Ecological Health of Raipur City, India. *Ecosyst. Heal. Sustain.*, Vol. 7(1). https://doi.org/10.1080/ 20964129.2021.1927852

[20] Al Kafy, A., Al- Faisal, A., Rahman, M. S., Islam, M., Al Rakib, A., Islam, M. A., Khan, M. H. H., Sikdar, S., Sarker, M. H. S., Mawa, J. and Sattar, G., (2021). Prediction of Seasonal Urban Thermal Field Variance Index Using Machine Learning Algorithms in Cumilla, Bangladesh. *Sustain. Cities Soc.*, Vol. 64. https://doi.org/10.1016/j.scs.2020.102542

[21] Al Kafy, A., Hasan, M. M., Al- Faisal, A., Nipun, W. H. and Noman, A. A., (2019). Estimation of Urban Heat Islands Effect and Its Impact on Climate Change: A Remote Sensing and GIS-Based Approach in Rajshahi District. *1st Int. Conf. Urban Reg. Planning, Bangladesh*, 560–569.

[22] Alfraihat, R., Mulugeta, G. and Gala, T. S., (2016). Ecological Evaluation of Urban Heat Island in Chicago City, USA. *J. Atmos. Pollut.*, Vol. 4(1), 23–29. https://doi.org/10.12691/jap-4-1-3

[23] Guha, S. and Govil, H., (2012). An Assessment on the Relationship between Land Surface Temperature and Normalized Difference Vegetation Index. *Environ. Dev. Sustain.*, Vol. 23(2). 1944–1963. https://doi. org/10.1007/s10668-020-00657-6

[24] Al- Faisal, A., Al Kafy, A., Al Rakib, A., Akter, K. S., (2021). Assessing and Predicting Land Use/Land Cover, Land Surface Temperature and Urban Thermal Field Variance Index Using Landsat imagery for Dhaka Metropolitan Area. *Environ. Challenges*, Vol. 4, 1-20. https://doi.org/10. 1016/j.envc.2021.100192

[25] Khan, M. S., Ullah, S. and Chen, L., (2021). Comparison on Land-Use/Land-Cover Indices in Explaining Land Surface Temperature Variations in the City of beijing, China. *Land*, Vol. 10(10). https://doi.org/10.3390/land101 01018

[26] Puri, M., Solanki, A., Padawer, T., Tipparaju, S. M., Moreno, W. A. and Pathak, Y., (2016). Introduction to Artificial Neural Network (ANN) as a Predictive Tool for Drug Design, Discovery, Delivery, and Disposition: Basic Concepts And Modeling. *Artificial Neural Network for Drug Design, Delivery and Disposition*. 3–13. https://doi.org/10.1016/B978-0-12 8015599.00001-6

[27] Effat, H. A., Taha, L. G. and Mansour, K. F., (2014). Change Detection of Land Cover and Urban Heat Islands Using Multi-Temporal Landsat Images, Application in Tanta City, Egypt. *Open J. Remote Sens. Position.*, Vol. 1(2). 1–15.

[28] El-Zeiny, A. M. and Effat, H. A., (2017). Environmental Monitoring Of Spatiotemporal Change in Land Use/Land Cover and Its Impact on Land Surface Temperature in El-Fayoum Governorate, Egypt. *Remote Sens. Appl. Soc. Environ.*, Vol. 8. 266–277.

[29] Mansour, K., Aziz, M. A., Hashim, S. and Effat, H., (2022). Impact of Anthropogenic Activitieson Urban Heat Islands in Major Cities of El-Minya Governorate, Egypt. *Egypt. J. Remote Sens. Sp. Sci.*, Vol. 25(2). 609–620. https://doi.org/10.1016/j.ejrs.2022.03.014

[30] Elnaggar, A. A., Azeez, A. A. and Mowafy, M., (2020). Monitoring Spatial and Temporal Changes of Urban Growth in Dakahlia Governorate, Egypt, by Using Remote Sensing and GIS Techniques. (Dept. C.(Public Works)). *MEJ. Mansoura Eng. J.*, Vol. 39(4), 1–14.

[31] Fonte, C. C., See, L., Laso-Bayas, J. C., Lesiv, M. and Fritz, S., (2020). Assessing the Accuracy of Land Use Land Cover (LULC) Maps Using Class Proportions in the Reference Data. *ISPRS Ann. Photogramm. Remote Sens. Spat. Inf. Sci.*, Vol. 5(3). https://doi.org/10.5194/isprs-annals-V-3-2020-669-2020

[32] Tucker, C. J., (1979). Red and Photographic Infrared Linear Combinations for Monitoring Vegetation. *Remote Sens. Environ.*, Vol. 8(2), 127–150.

[33] Sobrino, J. A., Raissouni, N. and Li, Z.-L., (2001). A comparative Study of Land Surface Emissivity Retrieval from NOAA Data. *Remote Sens. Environ.*, Vol. 75(2). 256–266.

[34] Zha, Y., Gao, J., and Ni, S., (2003). Use of Normalized Difference Built-Up Index in Automatically Mapping Urban Areas from TM Imagery. *Int. J. Remote Sens.*, Vol. 24(3). 583–594.

[35] McFeeters, S. K., (1996). The Use of the Normalized Difference Water Index (NDWI) in the Delineation of Open Water Features. *Int. J. Remote Sens.*, Vol. 17(7), 1425–1432.

[36] Isufi, F., Berila, A., Bulliqi, S., Khan, A., Chatterjee, S. and Wang, Y., (2021). Measuring UHI Using Landsat 8 OLI and TIRS Data with NDVI and NDBI in Municipality of Prishtina. *Disaster Adv.*, Vol. 14(11), 25–36.

[37] Khan, A., Chatterjee, S. and Weng, Y., (2021). UHI Drivers and Mapping the Urban Thermal Environment. *Urban Heat Isl. Model. Trop. Clim*, 69–115. https://doi.org/10.1016/ B978-0-12-819669-4.00003-9

[38] Valor, E. and Caselles, V., (1996). Mapping Land Surface Emissivity from NDVI: Application to European, African, and South American Areas. *Remote Sens. Environ.*, Vol. 57(3). 167–184.

[39] Sobrino, J. A., Caselles, V. and Becker, F., (1990). Significance of the Remotely Sensed Thermal Infrared Measurements Obtained Over a Citrus Orchard. *ISPRS J. Photogramm. Remote Sens.*, Vol. 44(6), 343–354.

[40] Sobrino, J. A., Jiménez-Muñoz, J. C. and Paolini, L., (2004). Land Surface Temperature Retrieval from LANDSAT TM 5. *Remote Sens. Environ.*, Vol. 90(4), 434–440

[41] Weng, Q., Lu, D. and Schubring, J., (2004). Estimation of Land Surface Temperature–Vegetation Abundance Relationship for Urban Heat Island Studies. *Remote Sens. Environ.*, Vol. 89(4), 467–483.

[42] Liu, L. and Zhang, Y., (2011). Urban Heat Island Analysis using the Landsat TM Data and ASTER Data: A Case Study in Hong Kong, *Remote Sens.*, Vol. 3(7), 1535–1552.

[43] Al Kafy, A., Al- Faisal, A., Rahman, M. S., Islam, M., Al Rakib, A., Islam, M. A., Khan, M. H. H., Sikdar, S., Sarker, M. H. S., Mawa, J. and Sattar, G., (2021). Prediction of Seasonal Urban Thermal Field Variance Index Using Machine Learning Algorithms in Cumilla, Bangladesh. *Sustain. Cities Soc.*, Vol. 64. https://doi.org/10.1016/j.scs.2020.102542

[44] Tepanosyan, G., Muradyan, V., Hovsepyan, A., Pinigin, G., Medvedev, A. and Asmaryan, S., (2021). Studying Spatial-Temporal Changes and Relationship of Land Cover and Surface Urban Heat Island Derived through Remote Sensing in Yerevan, Armenia. *Build. Environ.*, Vol. 187. https://doi.org/10.1016/j. buildenv.2020.107390

[45] Mansouri, I., Ozbakkaloglu, T., Kisi, O. and Xie, T., (2016). Predicting Behavior of FRP-Confined Concrete Using Neuro Fuzzy, Neural Network, Multivariate Adaptive Regression Splines and M5 Model Tree Techniques. *Mater. Struct.*, Vol. 49(10), 4319–4334.

[46] AlDousari, A. E., AlKafy, A., Milan Saha, M., Fattah, M. A., Almulhim, A. I., Al-Faisal, A., Al Rakib, A. A., Jahir, D. M. A., Rahaman, Z. A., Bakshi, A., Shahrier, A. and Md. Mijanur Rahman, M. M., (2022). Modelling the Mpacts of Land Use/Land Cover Changing Pattern on Urban Thermal Characteristics in Kuwait. *Sustain. Cities Soc.*, Vol. 86. https://doi.org/10.1016/j.scs.2022.104107.

[47] Amir Siddique, M., Wang, Y., Xu, N., Ullah, N. and Zeng, P., (2021). The Spatiotemporal Implications of Urbanization for Urban Heat Islands in Beijing: A Predictive Approach Based on CA–Markov Modeling (2004–2050). *Remote Sens.*, Vol. 13(22). https://doi.org/ 10.3390/rs13224697

[48] Kafy, A. A., Rahman, M. S., Hasan, M. M. and Islam, M., (2020). Modelling Future Land Use Land Cover Changes and their Impacts on Land Surface Temperatures in Rajshahi, Bangladesh. *Remote Sens. Appl. Soc. Environ.*, Vol. 18. https://doi.org/10.1016/j.rsase.2020. 100314

[49] Maduako, I. D., Yun, Z. and Patrick, B., Simulation and Prediction of Land Surface Temperature (LST) Dynamics within Ikom City in Nigeria Using Artificial Neural Network (ANN). *J. Remote Sens. GIS*, Vol. 5(1), 1–7.

[50] Van Gerven, M. and Bohte, S., (2017). Artificial Neural Networks as Models of Neural Information Processing. *Frontiers in Computational Neuroscience*, Vol. 11. https://doi.org/10.3389/fncom.2017.00114

[51] Fu, P. and Weng, Q., (2018). Responses of Urban Heat Island in Atlanta to Different Land-Use Scenarios. *Theor. Appl. Climatol.*, Vol. 133(1), 123–135.

[52] Lo, C. P. and Quattrochi, D. A., (2003). Land-use and land-Cover Change, Urban Heat Island Phenomenon, and Health Implications. *Photogramm. Eng. Remote Sens.*, Vol. 69(9), 1053–1063.

[53] Wang, H., Zhang, Y., Tsou, J. Y., and Li, Y., (2017). Surface Urban Heat Island Analysis of Shanghai (China) Based on the Change of Land Use and Land Cover. *Sustainability*, Vol. 9(9). https://doi.org/10.3390/su9091538

[54] Guha, S., (2021). Relationship between Land Surface Temperature and Normalized Difference Water Index on Various Land Surfaces : A Seasonal Analysis. Vol. 6(3), 165–173. https://doi.org/10.26833/ijeg.821730.

[55] Guha, S., (2020). Seasonal Contrast on the Correlation between Land Surface Temperature and Normalized Difference Water Index Using a Series of Landsat Data. *Int. J. Eng. Geosci.*, Vol. 6(3), 165–173. https://doi.org/ 10.26833/ijeg.821730

[56] Guha, S., Govil, H. and Besoya, M., An Investigation on Seasonal Variability between LST and NDWI in an Urban Environment Using Landsat Satellite Data. *Geomatics, Nat. Hazards Risk*, Vol. 11(1). 1319–1345. https://doi.org/10.1080/19475705.2020.1789762.